Published in Journal of Electron Spectroscopy and Related Phenomena 97, issue 3, 243-252, 1998
which should be used for any reference to this work

A monochromatized multiple energy laboratory UV source for **k**-space imaging

Th. Pillo*, L. Patthey[1], E. Boschung, J. Hayoz, P. Aebi, L. Schlapbach

Institut de Physique, Université de Fribourg, Pérolles, CH-1700 Fribourg, Switzerland

Abstract

A laboratory set-up for ultraviolet (UV) photoelectron spectroscopy combining a high intensity UV source and a toroidal UV monochromator, both being commercially available, is described. The source is modified in order to maximize the solid angle collected by the monochromator. Scanning its exit arm length allows for the optimization of the photon intensity as well as the energy resolution by minimizing the defocus term only. By using several different gases such as He, Ne or H_2 one obtains a powerful tool to sample extended regions in **k**-space. Fermi energy maps are presented for Cu(110) in the photon energy range from 10.2 to 48.3 eV. As a result of the variable photon energy an actual zooming into the well-known Shockley surface state is possible.

Keywords: Angle-resolved photoemission; Fermi surface mapping; Monochromatized UV radiation; **k**-Space mapping; Duoplasmatron

1. Introduction

Photoelectron spectroscopy provides direct information on the electronic properties of matter [1]. In particular, angle-resolved photoemission is *the* method for studying the energy and momentum distribution of electrons at and near surfaces. In the present set-up the idea is to map electronic states over as much as possible of the Brillouin zone (BZ) within reciprocal space. This so-called **k**-space mapping or imaging when displayed as a gray scale representation results in dispersion plots and cuts through constant energy surfaces, e.g. the Fermi surface (FS) [2–11]. Besides doing experiments as a function of emission angle it is highly desirable to vary the photon energy in order to access even wider regions within the BZ. Laboratory equipment has proven its power with respect to varying angles whereas synchrotron radiation facilities offer, in addition, a variable photon energy [12].

Laboratory sources have the disadvantage of relatively low intensities. The gas discharge also exhibits disturbing satellite side bands such that although excitations from noble gases show very narrow lines in photon energy additional low intensity lines with approximately the same energy occur (e.g. He Iα (21.2 eV) as the main line and He Iβ (23.1 eV) as the satellite line).

Consequently, one often has to struggle with disturbing features, e.g. in the proximity of the Fermi edge (E_F), due to intense features in the valence

* Corresponding author. Fax: + 41-26-300-9747; e-mail: thorsten.pillo@unifr.ch.

[1] Now at Swiss Light Source, CH-5232 Villigen-PSI, Switzerland.

band excited with a higher energy satellite line. It is not possible to simply subtract satellite-induced features since such transitions may stem from different locations in **k**-space. Additionally, satellite line intensities are highly sensitive to gas pressure. Therefore, a high intensity UV lamp combined with a UV monochromator, that allows one to *separate* these lines but with maximal transmission, is an excellent complement to synchrotron facilities.

In order to realize this, we have combined a commercially available high intensity UV lamp (UVS 300, formerly from Vacuum Science Instruments, now from SPECS GmbH, both Germany), which is based on the reverse duoplasmatron principle [13–15], with a UV monochromator (VUV 5040 from GammaData Burklint AB, Sweden). The advantage of this set-up is the capability of yielding a discharge with a vast number of gases, as for example He, Ne, Ar, or even H_2, thus covering UV energies ranging roughly from 10 to 50 eV [16].

The intermediate part of the UV lamp has been modified completely for the following two reasons. First, the UVS 300 lamp is based on a long quartz capillary. In order to adjust it correctly to the monochromator the capillary had to be removed. Second, in order to collect photons from a maximum solid angle on the toroidal grating monochromator, the opening of the plasma stage and the differential pumping had to be adjusted.

Great importance has been attached to the fact that, for a toroidal grating monochromator, different photon energies also require different geometries for the optical set-up since arm lengths and deflection angles have an optimum value [17]. However, a set-up allowing for the variation of all parameters would become impractical for a compact and high transmission design. Adjusting only the distance between grating and sample (exit arm length or image distance r'), thereby minimizing the defocus, by moving the whole set-up via a sliding carriage, we demonstrate the possibility of optimizing resolution and intensity at the same time.

The high performance of this set-up with respect to photoelectron spectroscopy will be illustrated with E_F mapping experiments performed on Cu(110). We report laboratory measurements with different photon energies, in particular with 10.2 eV (H Lyα), 11.3 eV, 12.1 eV (H Lyβ), 16.9 eV (Ne I), 21.2 eV (He Iα), 40.8 eV (He IIα), and 48.3 eV (He IIβ). The first three energies correspond to experimentally broadened lines of the H_2 quasi-continuum whereas the latter denote intrinsically sharp atomic excitation lines for the corresponding noble gases. By probing the Shockley surface state on Cu(110) with different photon energies we show that zooming into the BZ can definitely be realized.

The next section deals with our particular experimental set-up. Section 3 describes in detail the modifications to the UV lamp as well as the monochromator set-up. In Section 4 we present and discuss the photoemission measurements on Cu(110). We conclude our report in Section 5.

2. Experimental

The presented set-up provides a powerful extension of the existing photoelectron spectrometer (VG EscaLab Mk II), which has been modified before in order to perform angle-scanned photoemission measurements via motorized sequential sample rotation. Details have been described elsewhere [11,18,19]. Various different, in situ methods are provided in the spectrometer. The preparation chamber (base pressure 2×10^{-11} mbar) is equipped with a sputter gun, heating facilities, as well as with LN_2-cooled evaporation sources. Quality of samples can be checked with low energy electron diffraction (LEED). In addition, analysis with a scanning tunnelling microscope is possible in situ. The analysis chamber (base pressure 2×10^{-11} mbar) is supplied with an X-ray twin-anode (Mg Kα (1253.6 eV), Si Kα (1740 eV)). By means of the X-ray source photoelectron diffraction measurements are possible in order to perform structural studies [20,21]. Furthermore, using an ion gun for low energy ion scattering spectroscopy, it is possible to do angle-scanned ion scattering for structural studies of the topmost layers [22].

Polycrystalline samples and single-crystals used in this report have been prepared in standard fashion by several cycles of Ar^+-sputtering and subsequent annealing. Cleanness and surface quality have been checked by X-ray photoelectron spectroscopy and LEED, respectively.

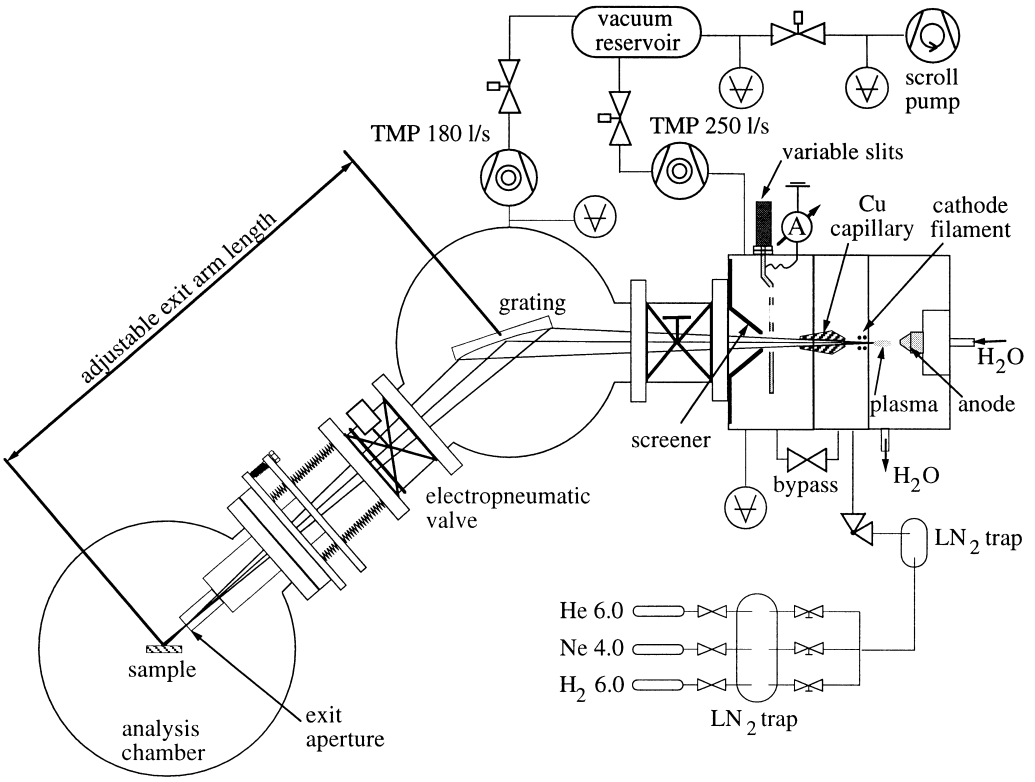

Fig. 1. Sketch of the experimental set-up of the UV lamp with monochromator. Note that it is not to scale. The two circles represent the analysis chamber and the monochromator chamber, respectively. The UVS 300 source is given schematically. For details see text.

3. UV source and monochromator

3.1. Instrumental set-up and UV source

The UV lamp and monochromator are made up of two main chambers, namely the lamp chamber and the monochromator chamber, the latter being described in the next subsection. In order to avoid contamination of the grating, an oil-free pumping system is used.

Fig. 1 shows a schematic set-up of the system. The pumping system consists of a Scroll pump (Varian 300DS), which is connected via an electropneumatic valve and a vacuum reservoir (volume 10 l) to the two turbomolecular pumps. The vacuum reservoir (Fig. 1) enables pressure controlled non-continuous operation of the Scroll pump to economize life time. The pumps are a 250 l/s (TMP 250) high flux pump for the differential pumping of the lamp and a 180 l/s (TMP 180) drag pump with a particularly high H_2 compression ratio. Resulting total gas pressures for the three relevant chambers during standard operation of the lamp are given in Table 1. Most importantly, pressures in the analysis chamber remain within the 10^{-9} mbar range and for hydrogen they are even below this value. The gas system connects the high purity gases via an LN_2 cold trap, leak valves, and another LN_2 cold trap (on the low pressure side of the leak

Table 1
Overview of the total pressures during operation of the UVS 300 source. Values are given for the *worst* case, meaning that all apertures are fully open. Pressures are uncorrected with respect to the sensitivity factors of the ion gauge/cold cathode

	Pressures [mbar]		
	Lamp	Monochromator	Analysis chamber
He	4×10^{-5}	3×10^{-6}	6×10^{-9}
Ne	2.5×10^{-5}	9.5×10^{-7}	1×10^{-9}
H_2	3×10^{-5}	2×10^{-6}	3×10^{-10}

valves) to the plasma chamber of the UVS 300 source. A choice of three different gases is available.

The lamp is based on the *reverse* duoplasmatron principle [13–15]. The *conventional* duoplasmatron was originally thought of as an ion source. Samson and Liebl [13] proposed its use as an ultraviolet radiation source. Principally it consists of an anode section and a cathode filament part (Fig. 1), which is able to provide high electron emission currents. Within an inhomogeneous magnetic field a plasma is created between anode and cathode. The advantage of the duoplasmatron with respect to conventional hollow cathode lamps is the considerably enhanced photon intensity [13,16]. The UVS 300 lamp is a conventional duoplasmatron with *reversed* geometry of anode and cathode, recently suggested by Gerhardt et al. [14,15]. The plasma ignites at a voltage of 150 V with corresponding cathode filament currents of about 20 A, depending on gas and pressure. The anode current can be set between 0 and 3 A, hence delivering photons approximately in proportion to the anode current. Gases are introduced into the plasma chamber between anode and cathode filament (Fig. 1). This plasma section is connected to the differential pumping stage (TMP 250) via a cylindrical copper capillary. It is also connected via a bypass valve to the pumping stage, providing improved pumping when the filament is initially degased after bakeout or before operation. For our set-up the cylindrical copper capillary has been replaced by a conical capillary modified in length [23] and for its opening angle in order to maximize the full solid angle and hence the illumination of the grating. With an entrance diameter of 2 mm a full solid angle of 5° is achieved. The pressures have been improved considerably with this new, longer capillary yielding, at the same time, an intensity enhancement of a factor of approximately 1.5 because it is reaching closer to the plasma region.

As sketched in Fig. 1, supplementary parts are added to the source. An entrance slit system can be used as the entrance aperture. Three different slits make the full solid angle switchable. In addition we can totally shut the entrance. A voltage can be applied to this shutter in order to avoid ions from the plasma on the grating or to measure the induced photocurrent. In order to improve pumping without losing solid angle a conically shaped screener is added (Fig. 1).

3.2. Monochromator and optics

Behind the screener and a gate valve, photons are diffracted by the toroidal grating and pass via another gate valve to the exit aperture and to the sample. The connection between this electropneumatic valve (Fig. 1) and the analysis chamber is made in such a manner that the whole set-up (including monochromator, lamp and turbo pumps) is movable on a sliding carriage. The reason for this adjustable exit arm length will be discussed below. The image of the source is optimized on the exit aperture with a diameter of 3 mm which is also movable independently with respect to the monochromator chamber. This exit aperture also has an important role minimizing the gas flux into the chamber (see Table 1). The monochromator grating is a laminar toroidal grating (1200 grooves/mm from Jobin-Yvon, France) optimized for He IIα radiation (40.8 eV) and second harmonics suppression. As a good compromise, the monochromator chamber itself has been optimized for He Iα radiation (21.2 eV) with respect to its entrance arm and deflection angle because the aim was also to use molecular hydrogen as discharge gas with energies in the range of 9–13 eV [16].

Following the review of West et al. [17] aberrations in the optical path function can be expressed by a sum over F_{ij} terms each representing a certain kind of aberration. For example, the first order terms F_{20}, F_{02}, F_{30} and F_{12} represent the defocus, astigmatism, coma and astigmatic coma terms, respectively. In the case of an ideal toroidal grating monochromator geometry, the entrance and exit arm lengths and the deflection angle should be adjusted for every photon energy to have the astigmatic term F_{02} equal to zero. This is, however, not possible in our case for reasons of space restriction. As a consequence of using different photon energies in a fixed geometry, one has to deal with large aberration and low energy resolution. An elegant alternative, therefore, is to optimize only the defocus term F_{20} which provides the largest contribution in the energy resolution power factor. This is done by varying solely the exit arm length whereas the entrance arm length and deflection angle stay constant. Then, the resolution power is significantly improved with respect to a fixed geometry. It should be noted that this scheme still provides a strong astigmatism since the astigmatic term F_{02} does not fulfill

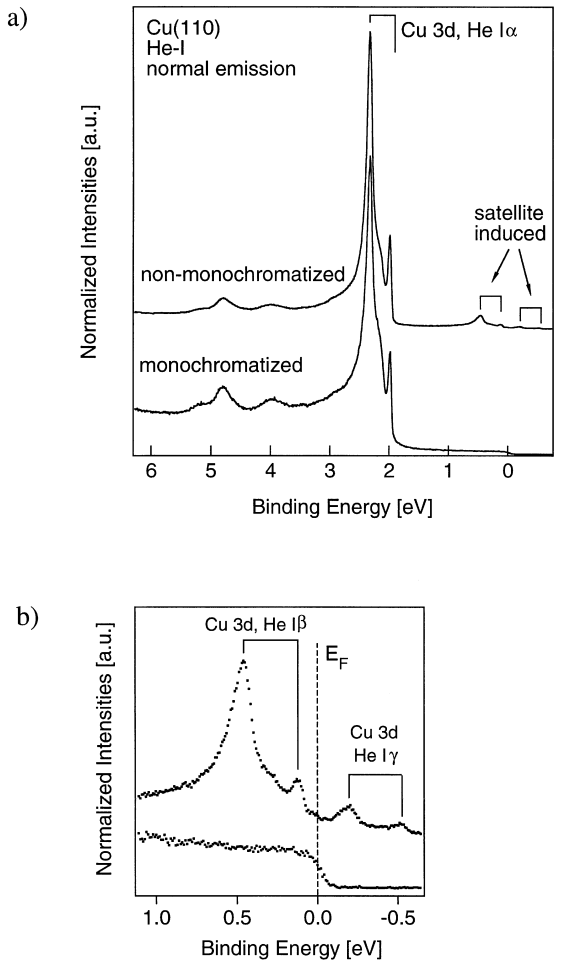

Fig. 2. (a) Comparison of ultraviolet photoemission spectra taken on Cu(110). Spectra have been normalized with respect to the *d*-band maximum. The spectrum measured without monochromator has been offset. (b) Same spectra as in (a) but only for the region around the Fermi edge.

the condition of the ideal toroidal grating geometry. However, for photoemission applications the crucial point is to separate different lines (i.e. the main line from the satellite) and not to have a perfect geometrical image of the source. In other words, we do not mind having a completely distorted geometrical image, as long as a maximal number of monochromatic rays concentrates in a minimal focus. Taking the example of He Iα, He Iβ and He Iγ photons (21.2, 23.1 and 23.8 eV, respectively), the center of gravity of the rays with different energies is at a constant

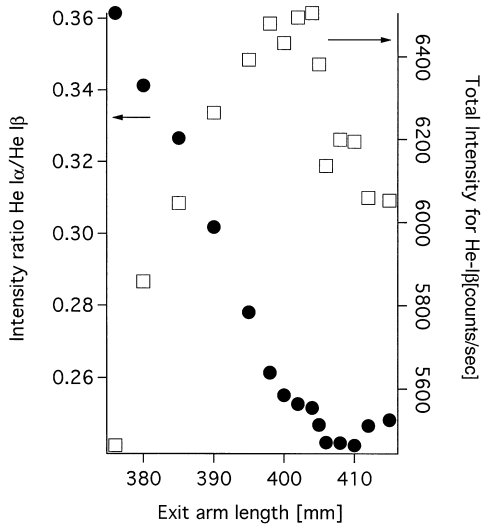

Fig. 3. Intensity ratio of spectral weight at E_F due to He Iα and He Iβ (left axis) and total intensity of the Fermi edge for He Iβ (right axis) as a function of the exit arm length. Note that the exit arm length corresponds to the actual image distance plus the distance from the sample to the exit aperture. Data is given for polycrystalline Ag.

angular separation given by the diffraction of the grating. What changes with r', however, is the distribution width of scattered rays and therefore their mixing. Optimizing the defocus term simply means to choose the exit arm length where rays of a given energy are focalized best, resulting in an optimal energy separation and resolution of the monochromator. This behavior is confirmed by ray-tracing calculations (not shown) for our set-up using the shadow program package.

4. Results and discussion

4.1. Performance of monochromator and lamp

First of all, in Fig. 2 we show a comparison of ultraviolet photoemission (UPS) spectra taken on Cu(110). Part (a) presents the overall valence band range with the strong Cu 3*d* band at approximately 2.5 eV binding energy. The top spectrum has been taken with the UVS 300 source without the monochromator (i.e. with the quartz capillary) whereas the bottom curve gives the same spectrum, but now

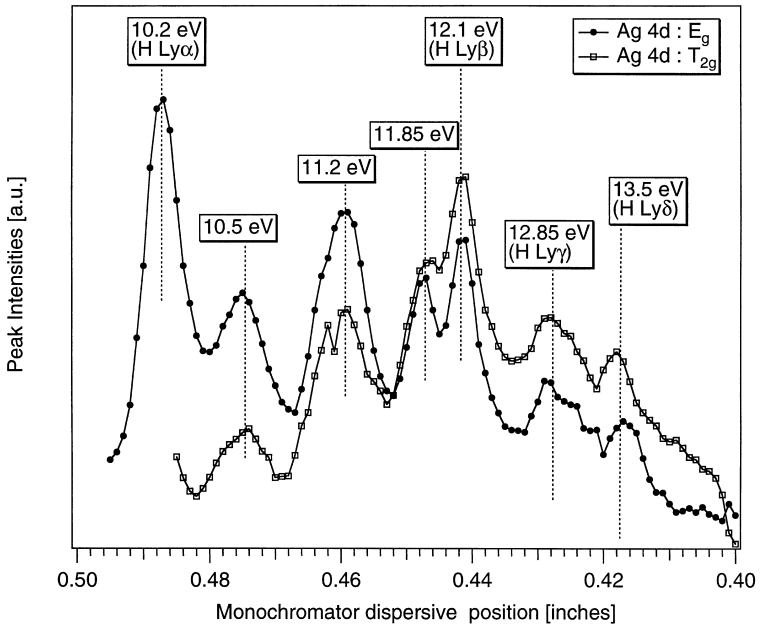

Fig. 4. Dispersive spectrum for H_2 discharge gas as obtained from the Ag polycrystal. Shown are the intensities for the two Ag 4*d* crystal field split T_{2g} and E_g bands as a function of the dispersive monochromator setting. Photon energies are labeled.

taken with monochromatized He Iα radiation. The smooth *sp*-band near E_F without satellites nicely demonstrates the performance of the set-up. As shown more strikingly in part (b), the Cu 3*d* band features around E_F induced by the He Iβ (23.1 eV) and the He Iγ (23.8 eV) satellite lines are, within the given accuracy, completely removed by the monochromator. In comparison, for 0th order diffraction, the intensity ratio He Iα/He Iβ is approximately 29.

In Fig. 3 we present calibration measurements demonstrating the efficiency of our r' optimization. Measurements have been performed on polycrystalline Ag, with the monochromator set for He Iβ radiation. The left axis gives the ratio between spectral weight at E_F due to He Iα and He Iβ (circles), and the right axis the total intensity of He Iβ excited spectral weight at E_F (squares), both as a function of the exit arm length. The monochromator has been set to He Iβ since the contribution of the near-lying very strong He Iα main line still gives a contribution within the same energy spectrum, thus allowing for a direct comparison with varying r'. As one can see in Fig. 3, a minimum is obtained in the He Iα/He Iβ intensity ratio at roughly 405 mm for r'. At the same time the intensity is also maximized.

The capability to distinguish between He Iα and He Iβ excited photoelectrons improves by about 30% ($[I_{max} - I_{min}]/I_{max}$ from the left axis). For the pure spectral weight at E_F one obtains an enhancement of 15% (from the right axis). This corresponds to the desired behavior. Note that the optimum position extends over several millimeters and the increase in the intensity ratio, as expected for going to larger arm lengths, cannot be seen clearly because our set-up is limited to a total distance of 415 mm. The rather asymmetric behavior, however, i.e. a steep decrease of the ratio followed by a flat region, is also reflected in the ray-tracing calculations. They show that the overlap of optical rays from the different energies does not significantly change when going to longer arms but, in contrast, mixing increases rapidly upon shortening the armlength. Furthermore, for the experiments shown in Fig. 3, the analyzer acceptance has been chosen such as to collect photoelectrons from the complete sample area that is illuminated through

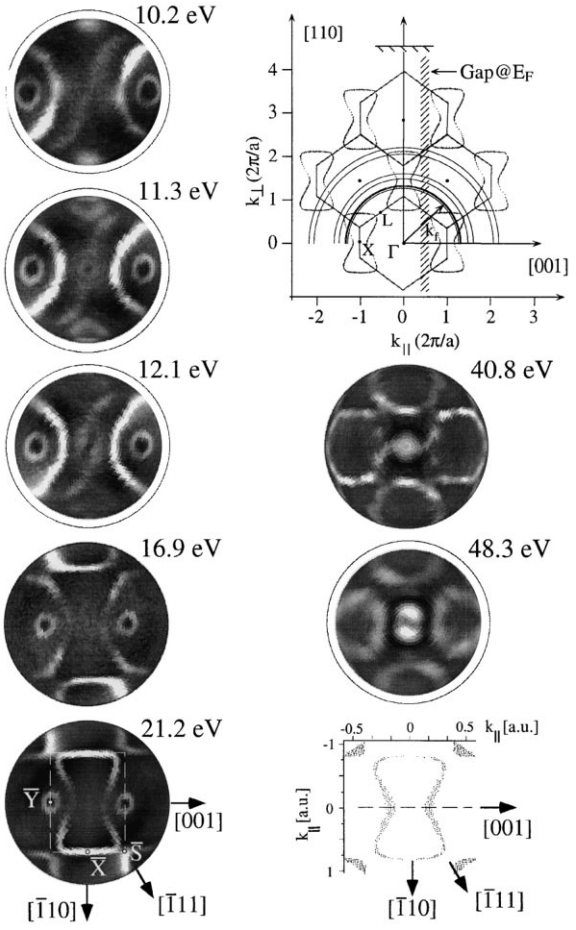

Fig. 5. Fermi surface mappings (FSM) for the Cu(110) single crystal. Photon energies are given. Left side: FSMs in the energy range where the Shockley surface state can be seen around $\bar{Y}$. Bottom left and right: experiment and theory for He Iα (21.2 eV). High symmetry points/directions and the SBZ are marked. The dashed line (bottom right) represents the cut sketched at the top right (cf. below): representation of the high symmetry plane perpendicular to the [$\bar{1}$10]-direction. Solid polygons represent the bulk BZ, dotted features give the result of the Cu FS calculation with typical necks and bones. With increasing radius $\mathbf{k}_f$ the circles around Γ represent the free electron final state wave vectors for 10.2, 11.3, 12.1, 16.9, 21.2, 40.8 and 48.3 eV.

the exit aperture (see Fig. 1). Reducing the analyzer acceptance area on the sample results in the disappearance of the He Iα signal demonstrating that by decreasing the exit aperture size the monochromator set-up easily separates both lines.

We focus now on the H_2-induced radiation. In Fig. 4 we present the Ag 4*d* photoelectron intensities for the photon energy region from 10 to nearly 14 eV. For every monochromator dispersive position a spectrum of the Ag 4*d* band was taken. By fitting its T_{2g} and E_g components, assuming two Gaussians and subtracting a Shirley background, we obtain energy position and intensity for every monochromator position. The maximum at 10.2 eV can be attributed to the very intense H Lyα line, whereas 12.1 eV corresponds to H Lyβ. Further maxima correspond to H Lyγ and H Lyδ and to photon energies given in the figure. Referring to the optical spectrum from Samson [16], our measured spectrum appears as a convolution of the sharp-lined optical spectrum with an experimental broadening. Notice that in this energy interval the Ag 4*d* photoabsorption cross section increases considerably towards higher photon energies. Therefore, intensities cannot be compared directly with the optical spectrum. The clear separation of several photon energies exhibits the possibility of using them for photoemission. However, due to the hydrogen quasi-continuum one always has a mixture of photon energies in the same photoemission spectrum for a given monochromator setting, which is expressed by a slightly smeared out Fermi edge[2]. The estimated energy resolution thus obtained is of the order of 200 meV at its best.

We conclude this section with a look at total photoelectron intensities provided by the monochromating system. With He photons of 0th order on the Ag polycrystal biased with -30 V we obtain a maximal sample current of 75 nA. Maximal sample currents of 28 and 8 nA are measured for He Iα (1st order) and He IIα (1st order), respectively. All values have been obtained for an anode current of 3 A of the UVS 300 source. They have been optimized with respect to the gas pressure and the cathode filament current. For hydrogen and neon, sample currents of the same order of magnitude were obtained.

Regarding the photoelectron intensities of the Cu 3*d* band maximum for He Iα at 1 A anode current, we find a factor of about 2 less intensity with the monochromator compared to the original UVS 300 UV

[2] The measured Fermi edge is broadened and can be successfully fitted with two Fermi–Dirac distributions being slightly different in energy positions.

source with a 160 mm quartz capillary (2 mm diameter) at the same anode current. Compared to our previous Leybold UV source operated without monochromator we obtain a factor of 1.5 more in monochromatized intensity at 1 A. Given the fact that operation at 3 A is possible we gain more than a factor of 4. Our laboratory set-up therefore provides monochromatized photons of various energies with high intensity.

*4.2. **k**-space imaging*

We focus now on the physical relevance of this new set-up with regard to photoelectron spectroscopy. In Fig. 5 we present a set of Fermi surface mappings (FSM) measured on the Cu(110) surface using different photon energies. Two-dimensional cuts through the three-dimensional FS of Cu have been described in detail for 21.2 eV radiation elsewhere [3].

Briefly, the photoelectron intensity is collected within a small energy window centered at E_F. This spectral weight is mapped for all emission angles and displayed in a linear gray scale representation as a function of the parallel component ($k_\parallel$) of the wave vector **k** according to the well-known photoemission formula (for zero binding energy)

$$k_\parallel\left[\text{Å}^{-1}\right] = 0.512\cdot\sqrt{\hbar\omega[\text{eV}] - \phi[\text{eV}]}\times\sin\vartheta \qquad (1)$$

where $\hbar\omega$ and ϕ denote the photon energy and the work function, respectively. The center of the mappings represents normal emission ($\vartheta = 0°$) whereas the outer circles represent grazing emission ($\vartheta = 90°$).

The bottom of Fig. 5 compares the He Iα (21.2 eV) FSM (left) with a calculation [3] (right) done within the Layer–Korringa–Kohn–Rostocker (LKKR) formalism [24] indicating the intensity contributions (black dots) due to direct transitions from E_F in the frame of the free electron final state (FEFS) approximation. The surface Brillouin zone (SBZ) is sketched and high symmetry points and directions are labeled. Within the FEFS approximation high photoelectron intensities appear in the experiment for direct transitions between the FS in the extended zone scheme and the FEFS sphere accounting for energy and momentum conservation. This is illustrated in the top right drawing of Fig. 5. Assuming an inner potential of $V_0 = 13.5$ eV and a work function of $\phi = 4.7$ eV, we draw the FEFS wave vectors $k_f = 0.512\cdot\sqrt{\hbar\omega[\text{eV}] - \phi[\text{eV}] + V_0[\text{eV}]}$ as circular segments around the Γ-point of the bulk BZ. The length of the final state vectors increases with the photon energy, corresponding to 10.2, 11.3, 12.2, 16.9, 21.2, 40.8 and 48.3 eV. The solid line hexagons represent the bulk BZ. Partly dotted is the result of the FS calculation, exhibiting the well-known 'necks' at the *L*-points and 'bones' around *X*. From this sketch one can see that different photon energies lead to different cuts, therefore slicing through the bulk FS.

The most eyecatching feature is the well-known Shockley surface state around the $\bar{Y}$-point of the SBZ. As a matter of fact, the surface state appears in regions of the bulk gap as is indicated in the top right sketch of Fig. 5 by the hatched area. A zooming effect can be seen very nicely when reducing the photon energy from 21.2 down to 10.2 eV. This is easy to explain taking into account the usual photoemission formula of Eq. (1) where changing the photon energy $\hbar\omega$ modifies the expression for $k_\parallel$. The $k_\parallel$ range covered within 0–90° of emission angles becomes smaller for decreasing photon energies. Therefore, in order to scan the existence area of the $\bar{Y}$ surface state, i.e. the hatched area (Fig. 5, top right) of the bulk gap, the angular interval increases for lowering the photon energy, thus explaining the zooming effect. The same applies to bulk states where with increasing photon energy the FEFS vector $\mathbf{k}_f$ reaches farther out. As a result, going from $\hbar\omega = 10.2$ to 21.2 eV, the strong half-ellipses centered around the Shockley states continuously move towards the center. Differences in spectral weight along the high intensity lines are explained by matrix element effects, including the influence of the polarization. At present the origin of the weak propeller-like features crossing the center of the H_2 FSMs (10.2, 11.3 and 12.1 eV) is unclear. They have more or less the same symmetry as the bulk bands and correspond most probably to excitations with a slightly different photon energy as explained before (see the previous footnote).

The two He II FSMs (40.8 and 48.3 eV) are quite different from those for energies below 21.2 eV. Now the final state wave vector is large compared to the dimensions of the SBZ and, hence, the $k_\parallel$ resolution is

worse. The Shockley surface state is not resolved anymore, a fact that may be attributed to cross section effects. On the other hand, a wider region in **k**-space is accessible at these energies. The final state sphere touches the FS near normal emission at the top of the 'dog-bone' (Fig. 5, top right), such as to produce an extended area of high intensity.

Finally we may notice that gray scale mapping is not restricted to constant energy scans as presented in Fig. 5 but is also applicable for collecting complete energy distribution curves along high symmetry directions as reviewed for the textbook example Cu in Fig. 4 of Ref. [11]. Other examples are given for Ni(111) [9], c(2 × 2) − Na/Al(001) [25], Yb/Al(001) [26] or H/Ni(110) [27]. The two measuring modes nicely illustrate the inherent complement between the **k**(*E*) and *E*(**k**) way of displaying band structures, therefore justifying the term '**k**-space imaging'.

5. Conclusions

We have presented a new experimental set-up combining a high intensity UV source and a VUV monochromator for photoelectron spectroscopy. The possibility of scanning the exit arm length allows one to optimize resolution and intensity at the same time. A great variety of different photon energies is obtained depending on the discharge gas. In particular, using H_2, a quasi-continuum of photon energies arises between 10 and 13 eV. The set-up, therefore, provides a powerful tool for angle-resolved photoelectron spectroscopy, as shown by an actual zooming into the surface BZ of Cu(110), demonstrating real **k**-space imaging.

Acknowledgements

We are indebted to Prof. U. Gerhardt from the University of Frankfurt/Main (Germany) for many helpful discussions and hints. In addition, we would like to thank Drs J. Thomassen and K. Oswald from VSI Germany. We thank D. Naumović for fruitful discussions. Furthermore, we gratefully acknowledge the excellent technical assistance by E. Mooser, O. Raetzo, O. Zosso, R. Vonlanthen, F. Bourqui and C. Neururer. This work has been supported by the Fonds National Suisse pour la Recherche Scientifique.

References

[1] S. Hüfner, Photoelectron Spectroscopy, Springer Series in Solid State Sciences 82, Springer, Berlin, 1995.
[2] A. Santoni, L.J. Terminello, F.J. Himpsel, T. Takahashi, Appl. Phys. A52 (1991) 229.
[3] P. Aebi, J. Osterwalder, R. Fasel, D. Naumović, L. Schlapbach, Surf. Sci. 307–309 (1994) 917.
[4] P. Aebi, J. Osterwalder, P. Schwaller, L. Schlapbach, M. Shimoda, T. Mochiku, K. Kadowaki, Phys. Rev. Lett. 72 (1994) 2757.
[5] A.P.J. Stampfl, J.A. Con Foo, R.C.G. Leckey, J.D. Leckey, J.D. Riley, R. Denecke, L. Ley, Surf. Sci. 331–333 (1995) 1272.
[6] J. Avila, C. Casado, M.C. Asensio, J.L. Perez, M.C. Muñoz, F. Soria, J. Vac. Sci. Technol. A13 (1995) 501.
[7] Z. Qu, A. Goonewardene, K. Subramanian, J. Karunamuni, N. Mainkar, L. Ye, R.L. Stockbauer, R.L. Kurtz, Surf. Sci. 324 (1995) 133.
[8] P. Aebi, T.J. Kreutz, J. Osterwalder, R. Fasel, P. Schwaller, L. Schlapbach, Phys. Rev. Lett. 76 (1996) 1150.
[9] T. Greber, T.J. Kreutz, J. Osterwalder, Phys. Rev. Lett. 79 (1997) 4465.
[10] T. Greber, O. Raetzo, T.J. Kreutz, P. Schwaller, W. Deichmann, E. Wetli, J. Osterwalder, Rev. Sci. Instrum. 68 (1997) 4549.
[11] P. Aebi, R. Fasel, D. Naumović, J. Hayoz, Th. Pillo, M. Bovet, R.G. Agostino, L. Patthey, F.P. Gil, H. Berger, T.J. Kreutz, J. Osterwalder, L. Schlapbach, Surf. Sci. 402–404 (1998) 614.
[12] C.S. Fadley, in: R.Z. Bachrach (Ed.), Synchrotron Radiation Research: Advances in Surface Science, Plenum, New York, 1993.
[13] J.A.R. Samson, H. Liebl, Rev. Sci. Instr 33 (1962) 1340.
[14] B. Dötsch, J. Thomassen, U. Gerhardt, in: Proceedings of the 42nd AVS National Symposium, Minneapolis, USA, 1995.
[15] S. Marquardt, Diploma Work, University of Frankfurt/Main, Germany, 1991.
[16] J.A.R. Samson, Techniques of Vacuum Ultraviolet Spectroscopy, John Wiley & Sons, New York, 1967.
[17] J.B. West, H.A. Padmore, in: Handbook on Synchrotron Radiation, Volume 2, North-Holland Publishing, 1987, p. 21.
[18] D. Naumović, A. Stuck, T. Greber, J. Osterwalder, L. Schlapbach, Phys. Rev. B 47 (1993) 7462.
[19] J. Osterwalder, T. Greber, A. Stuck, L. Schlapbach, Phys. Rev. B 44 (1991) 13764.
[20] R. Fasel, P. Aebi, L. Schlapbach, J. Osterwalder, Phys. Rev. B 52 (1995) R2313.
[21] R. Fasel, P. Aebi, R.G. Agostino, D. Naumović, J. Osterwalder, A. Santaniello, L. Schlapbach, Phys. Rev. Lett. 76 (1996) 4733.
[22] R.G. Agostino, P. Aebi, J. Osterwalder, J. Hayoz, L. Schlapbach, Surf. Sci. 384 (1997) 36.
[23] U. Gerhardt, private communication, 1998.

[24] J.M. MacLaren, S. Crampin, D.D. Vvedensky, R.C. Albers, J.B. Pendry, Comput. Phys. Commun. 60 (1990) 365.
[25] R. Fasel, P. Aebi, R.G. Agostino, L. Schlapbach, J. Osterwalder, Phys. Rev. B 54 (1996) 5893.
[26] R. Fasel, P. Aebi, J. Osterwalder, L. Schlapbach, Surf. Sci. 394 (1997) 129.
[27] E. Boschung, Th. Pillo, J. Hayoz, L. Patthey, P. Aebi, L. Schlapbach, Phys. Rev. B58 (1998) R10210.